Reynolds flux modeling; new numerical insights into inclined dense jets

Sina Tahmooresi[1*], Abdolmajid Mohammadian[1†], Ioan Nistor[1†] and Hossein Kheirkhah Gildeh[†]

[1*]Department of Civil Engineering, University of Ottawa, 75 Laurier Ave E, Ottawa, K1N 6N5, ON, Canada.

*Corresponding author(s). E-mail(s): stahm017@uottawa.ca;
†These authors contributed equally to this work.

Abstract

This paper aims to provide a more detailed representation of the scalar flux modeling (SFM) approach for modeling turbulent inclined negatively buoyant jets. The SFM approach addresses the limitations of eddy viscosity models in terms of the mean concentration field and turbulent scalar flux within the context of Reynolds-averaged Navier-Stokes modeling. In this study, the contribution of the involved terms in the transport equation of the turbulent scalar flux vector was evaluated, and the geometrical and mixing parameters of concentration and velocity of 45° inclined negatively buoyant jets were verified. The SFM approach, along with the required modification for momentum flux modeling, was implemented in OpenFOAM v6. Results showed that the SFM approach can accurately predict mixing parameters due to the complex interactions between different turbulence contributors of the flow involved in the model. In comparison to simpler approaches, such as gradient-type models, that only correlate the gradient of the scalar field with turbulence, the SFM approach's capability to predict mixing parameters is significantly higher.

Keywords: Mixing, Inclined negatively buoyant jets, Turbulent scalar flux, Boussinesq approximation

1 Introduction

In an inclined dense jet that rises upward, as a result of the initial momentum, the jet rises to a terminal rise height and then falls to the source (nozzle) level due to the negative buoyancy. Subsequently, it spreads as a density current. Efficient mixing of a dense effluent discharge with the receiving ambient has made the inclined dense jets a popular configuration for brine discharge [1]. Inclination causes a longer trajectory and a higher dilution and makes the flow not fall back directly onto itself [2]. Figure 1 illustrates a schematic view of an inclined negatively buoyant jets (INBJ) on its symmetrical plane and its conventionally important parameters for environmental regulations. One key parameter to characterize the behavior of a jet with negative buoyancy is densimetric Froude number defined as

$$Fr = \frac{U_0}{\sqrt{g(\frac{\rho_0 - \rho_a}{\rho_a})D}} \tag{1}$$

where U_0 is the initial jet velocity at the nozzle, D is the nozzle diameter, and g is the gravitational acceleration; ρ_0 and ρ_a are the density of the jet and receiving ambient, respectively.

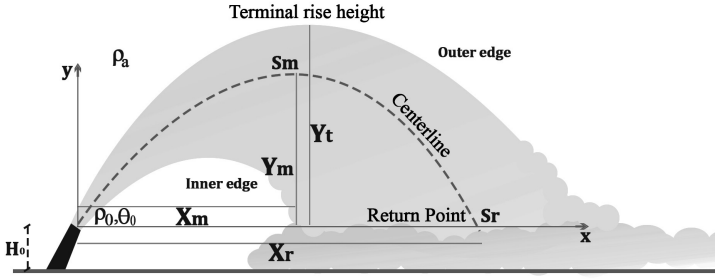

Fig. 1 Schematic view of an inclined dense jet and its environmentally important parameters

With regard to the angle of inclination and those environmentally important parameters consisting of geometrical (X_m as the horizontal distance of the centerline peak to the origin, Y_m as the vertical distance from the centerline peak to the nozzle elevation, Y_t as the terminal rise height, and X_r as the jet return point) and mixing (S_m and S_r as dilution ratios at the centerline and return point, respectively), several experimental investigations were conducted. These studies frequently reported their measurement with respect to the bulk parameters of the flow ([2–20]). Environmentally important parameters aside, the least attention was paid to the turbulence characteristics of INBJs. The only turbulence parameter reported in a group of studies is concentration fluctuation (e.g., [8, 10, 11]). Moreover, Crowe [21] reported the shear stress component of Reynolds stress tensor for INBJ. A lack of data

on Reynolds stress measurements prevents advance models calibration from further improvements in numerical modeling of INBJs [22].

Numerical modeling of INBJs can be categorized into three areas as analytical, integral, and models based on computational fluid dynamics (CFD) known as CFD models. Analytical models may equivalently be seen as length-scale models. These models are developed based on using non-dimensional numbers with which flow behavior can be classified into different regimes [23]. CORMIX [24], which is one the most frequently used models in near-filed prediction of the INBJs, is a length-scale model. These models provide the least detailed solution due to their simplicity and the limitation roots in the range of the experimental data used in model calibration process [25]. However, despite the simplifications, the capability of these models to demonstrate acceptable accuracy in prediction of trajectory parameters should be acknowledged. Recently, an analytical model approach was developed by Papakonstantis and Christodoulou [26] based on using an extensive experimental data. They proposed polynomial expression for INBJ trajectory for inclination between 35° to 75°. Moreover, minimum dilution at key points of maximum centerline height and return point were related to the computed length of the trajectory.

Integral models numerically integrate a system of equations for mass, momentum, and buoyancy flux using simplifying assumption for the closure problem [27]. These models have been investigated for decades. Using entrainment closure approach, first-order jet integral models were developed in pioneering works of Morton et al. [28] and Fan [29], while improvement were made in second-order integral models that can be found in studies of Wang and Law [30], Jirka [31], and Yannopoulos [32]. Oliver et al. [33] used reduced buoyancy flux (RBF) to improve the integral model of Yannopoulos and Bloutsos [34], where they hired escaping mass approach (EMA) for their integral model. The RBF model of Oliver et al. [33] was further investigated and improved in the context of modified RBF by Crowe et al. [27]. They used local parameters to determine the loss of buoyancy flux over the full trajectory and not only till the flow reaches the terminal height as is in the RBF. The EMA approach was revisited in the recent work of Bloutsos and Yannopoulos [35], applying the EMA over a broad range of inclinations ($15° - 75°$) and Fr numbers ($4 - 100$). They emphasized that EMA model is capable of reliable prediction of the flow parameters (geometrical and mixing), while the cost of computation is low as an integral model. Very recently, a comparative study by Papakonstantis and Papanicolaou [36] was conducted to compare five different numerical approach (including integral modeling with EMA and two different entrainment approaches, commercial code, Corjet [31, 37], and an analytical model proposed by Kikkert et al. [6]) for INBJs modeling.

In simulating INBJs using CFD, two approaches have been used: Reynolds-averaged Navier-Stokes (RANS) equations and Large-eddy simulation (LES).In RANS studies, both eddy viscosity models (EVM) and Reynolds stress models (RSM) have been employed (e.g., [22, 38–43]), with most studies

focusing on Reynolds stress modeling, compared to the Reynolds flux modeling (SFM). This challenge was addressed in the study of Tahmooresi and Ahmadyar [22], where they used SFM approach to model the turbulent flux vector.

Several studies have utilized Large-eddy simulation (LES) approach for simulating INBJs (e.g., [44–49]). These studies have demonstrated that LES can effectively predict the geometrical features of the flow, in good agreement with experimental data. However, for the mixing parameters, LES results were often reported to be less accurate than the geometrical ones. Vafa et al. [49] suggested that the discretization scheme of the convection terms significantly affects the accuracy of the mixing results.

In all above-mentioned LES studies as well as those that employed RANS, standard gradient diffusion hypothesis (SGDH) was used. SGDH approach is the simplest way to model the Reynolds flux vector. With respect to the numerical investigations reporting INBJs modeling, there is an underestimation of dilution ratios in nearly all numerical models, specifically at the return point. However, the range of this under prediction varies between more than 50% in some commercial codes with integral modeling approach ([50]) and 20% in the LES modeling of 45° inclined dens jets ([44], [45], [47]). Employing the regional turbulent Schmidt number (RTSN) approach, [42] reduced this underestimation to $\sim 14\%$ at the return point for 45° inclined dens jets. Vafa et al. [49] addressed the problem of underestimation of dilution in LES by changing the discretization schemes for convective terms of the filtered momentum and scalar transport equations.

In their study, Tahmooresi and Ahmadyar [22] aimed to improve RANS modeling beyond EVM using second-moment closure for Reynolds flux modeling which resulted in a good agreement with experimental data. The simulation was also able to successfully verify concentration fluctuations. Their simulation was comparable to LES models but required significantly fewer grids. The methodology is further discussed in their study [22].

The purpose of this paper is to provide additional information about scalar flux modeling (SFM) and how it can improve the accuracy of mean concentration field predictions in RANS modeling, as compared to eddy viscosity models (EVM). The primary focus of this paper is to investigate the various terms involved in the transport equation of the turbulent scalar flux vector and their contribution to the overall SFM approach.

The remaining of the paper is organized as follows. under the section 2, the governing equations and the Reynolds flux modeling are introduced as part of the closure problem. Then, simulation and related setups in OpenFOAM are followed in section 3. Under the section 4, it was tried to cover the main objectives of the paper through a comprehensive report on the turbulence characteristics as well as the bulk parameters of the results. Finally, to wrap up, section 5 is provided with remarks on the most important conclusions of the study.

2 Theoretical aspects

2.1 Governing equations

2.1.1 Reynolds-averaged Navier-Stokes equations

Using the Reynolds decomposition method, which results in Reynolds-averaged Navier-Stokes (RANS) equations, the averaged equations can be used to predict turbulent flows. With RANS, the governing equations for three-dimensional unsteady incompressible fluid flows can be written as follows [51]

$$\frac{\partial U_i}{\partial x_i} = 0 \tag{2}$$

$$\frac{\partial U_i}{\partial t} + \frac{\partial (U_i U_j)}{\partial x_j} = \frac{-1}{\rho_r}\frac{\partial P}{\partial x_i} + \frac{\partial \tau_{ij}}{\partial x_j} - \frac{\partial \overline{u_i' u_j'}}{\partial x_j} + g_i \frac{\Delta \rho}{\rho_r} \tag{3}$$

$$\frac{\partial \Phi}{\partial t} + \frac{\partial (\Phi U_j)}{\partial x_j} = \frac{\partial}{\partial x_j}(\Gamma \frac{\partial \Phi}{\partial x_j}) - \frac{\partial \overline{u_j' \phi'}}{\partial x_j} + S_\Phi \tag{4}$$

where the viscous stress tensor can be shown as

$$\tau_{ij} = \nu(\frac{\partial U_i}{\partial x_j} + \frac{\partial U_j}{\partial x_i}) - \frac{2}{3}\nu \delta ij(\frac{\partial U_k}{\partial x_k}) \tag{5}$$

where U_j is velocity, P is pressure, g is the gravitational acceleration, ρ_r is the reference fluid density ($= \rho_a$), S_Φ is a source term, and Φ is a scalar quantity, which can be represented by concentration (salinity), temperature, turbulent kinetic energy (k), and its dissipation rate (ϵ) in EVMs. Γ is the molecular diffusivity, and ν is the molecular viscosity. Moreover, $\overline{u_i' u_j'}$ and $\overline{u_j' \phi'}$ represent the Reynolds stress tensor and Reynolds flux (turbulent scalar flux) vector, respectively.

Since discharge applications deal with ocean and seawater as the receiving body, density variation is assumed to be a function of concentration and temperature using the following equation of state [52]

$$\rho = \rho_t + AS + BS^{\frac{3}{2}} + CS^2 \tag{6}$$

where ρ_t, A, and B include T (temperature), S represents concentration, and C is a constant value.

The most important aspect of the RANS system of equations is to estimate the Reynolds stresses and Reynolds fluxes to solve the closure problem, i.e., turbulence modeling, which is discussed in the following.

2.1.2 Reynolds flux modeling

In equation (4), turbulent scalar flux vector, $\overline{u_j' \phi'}$, should be modeled as part of the closure problem. The simplest way to do this is to use Fick's law to

simply relate the turbulent scalar flux to gradient of the mean scalar field

$$\overline{u_j'\phi'} = -\Gamma_t \frac{\partial \Phi}{\partial x_j} \tag{7}$$

where Γ_t is the eddy diffusivity and can be related to the eddy viscosity through turbulent Schmidt/Prandtl number

$$\Gamma_t = \frac{\nu_t}{Sc_t} \tag{8}$$

where ν_t and Sc_t represent eddy viscosity and turbulent Schmidt number, respectively. Equation (7), thus, is a gradient-type model and referred to as standard gradient diffusion hypothesis (SGDH) in the literature. The main problem with such a simple gradient-type model is that they consider no dependencies on turbulence parameters as well as the mean-velocity gradient of the flow. This model also neglects the ansiotopy of turbulence as it implicitly assumes the alignment of the turbulent scalar flux and the mean scalar gradients. One way to tackle the anisotropy problem of the SGDH model is to generalize the gradient-transport hypothesis by defining a diffusivity tensor [53]:

$$\overline{u_i'\phi'} = D_{ij} \frac{\partial \Phi}{\partial x_i} \tag{9}$$

where D_{ij} is the diffusivity tensor introduced by Batchelor [54]. Daly and Harlow [55] related the D_{ij} to the Reynolds stress tensor in generalized gradient diffusion hypothesis (GGDH)

$$\overline{u_i'\phi'} = -\frac{3}{2}\frac{C_\mu}{Sc_t}\frac{k}{\epsilon}\overline{u_i'u_j'}\frac{\partial \Phi}{\partial x_j} \tag{10}$$

where C_μ is constant equal to 0.09. Although neglected in most of the reported forms of the RANS equation for scalar transport, Reynolds flux can be modeled implicitly using a similar method used to derive the Reynolds stress equation (more details can be found in [56]). The resulted equation, in a very similar form to the Reynolds stress transport equation, can be written as [51, 56]

$$\begin{aligned} &\underbrace{\frac{\partial \overline{u_i'\phi'}}{\partial t}}_{\text{i}} + \underbrace{U_l \frac{\overline{u_i'\phi'}}{\partial x_l}}_{\text{ii}} = \underbrace{-\left[\overline{u_i'u_j'}\frac{\partial \Phi}{\partial x_j} + \overline{u_j'\phi'}\frac{\partial U_i}{\partial x_j}\right]}_{\text{(iii)}} \underbrace{-\beta g_i \overline{\phi'^2}}_{\text{(iv)}} + \underbrace{\frac{1}{\rho}\overline{p'\frac{\partial \phi'}{\partial x_i}}}_{\text{(v)}} \\ &\underbrace{-\frac{\partial}{\partial x_l}\left(\overline{u_i'u_l'\phi'} + \frac{1}{\rho}\delta_{il}\overline{p'\phi'}\right)}_{\text{(vi)}} \underbrace{-(\Gamma+\nu)\overline{\frac{\partial u_i}{\partial x_l}\frac{\partial \phi'}{\partial x_l}}}_{\text{(vii)}} \end{aligned} \tag{11}$$

where terms (i) and (ii) represent the rate of change and convective transport of the $\overline{u_i'\phi'}$, respectively. Terms (iii) and (iv) acount for production of

$\overline{u_i'\phi'}$ due to the turbulent interaction with the mean velocity and scalar field, and the gravitational forces (i.e., production due to the buoyancy), respectively [53]. Term (v) is responsible for the pressure-scalar correlation, which can be regarded as the counterpart of the pressure-strain term in Reynolds stress equations [57]. Remaining terms (vi) and (vii) are the diffusive (spatial) transport of the scalar due to the fluctuations of the velocity and pressure, and viscous destruction, respectively [51, 57].

Concerning the equation (11), concentration fluctuations, mean- square scalar variance, $\overline{\phi'^2}$, can be considered as the counterpart of turbulent kinetic energy (TKE), with regard the appearance of the equation [56].

$$\underbrace{\frac{\partial \overline{\phi'^2}}{\partial t}}_{\text{rate of change}} + \underbrace{U_j \frac{\partial \overline{\phi'^2}}{\partial x_j}}_{\text{convection}} = \underbrace{-\frac{\partial}{\partial x_j}\overline{u_j'\phi'^2}}_{\text{diffusion}} \underbrace{-2\overline{u_j'\phi'}\frac{\partial \Phi}{\partial x_j}}_{\text{production}} \underbrace{-2\Gamma\overline{\frac{\partial \phi'}{\partial x_j}\frac{\partial \phi'}{\partial x_j}}}_{\text{dissipation}} \tag{12}$$

The last term in this equation, known as ϵ_ϕ, $-2\Gamma\overline{\frac{\partial \phi'}{\partial x_j}\frac{\partial \phi'}{\partial x_j}}$, is the viscous dissipation due to the concentration fluctuation productions and, similarly, can be seen as the counterpart of the dissipation of turbulent kinetic energy, ϵ, for the Reynolds stresses. As ϵ is a challenging term to be modeled, ϵ_ϕ also imposes its difficulties on the set of equations and needs to be treated carefully. Similar to the ϵ equation, a transport equation for ϵ_ϕ may be written for this term [56] (the equation is not mentioned for the sake of brevity). For the purpose of this research, another proposal, which is more applicable, implementable, and frequently reported in the literature, to model the ϵ_ϕ was used. In this regard, Launder [57] suggested that dissipation of the scalar fluctuations in equation (12) is proportional to the dissipation rate of turbulent kinetic energy (ϵ) [51]

$$\epsilon_\phi = \frac{\overline{\phi'^2}}{kR}\epsilon \tag{13}$$

where R is the ratio of dynamic to scalar time scales [58]. Rodi [51] emphasized that R varies between 0.5 and 1.0 depending on the type of the flow. A value of 0.8 used for the purpose of the present study. However, it was shown in [22] that a dynamic configuration of this parameter leads to the best agreement with the experimental data. In equation (12), the diffusion term can be represented by a gradient-type model [51]

$$-\overline{u_j'\phi'^2} = c_\phi \frac{k}{\epsilon}\overline{u_j'u_l'}\frac{\partial \overline{\phi'^2}}{\partial x_l} \tag{14}$$

where c_ϕ is an empirical constant that must be determined experimentally.

As suggested by Launder [57], neglecting the diffusive transport by pressure fluctuations and relating it only to the velocity fluctuations, diffusive transport term, term (vi) in equation (11), can be modeled using a gradient-type model.

However, it usually contributes the least into the Reynolds flux equation as is neglected in algebraic stress models [53]. Term (vi) can thus be modeled as

$$-\frac{\partial}{\partial x_l}(\overline{u_i' u_l' \phi'} + \frac{1}{\rho}\delta_{il}\overline{p'\phi'}) = \frac{\partial}{\partial x_l}[c_{s\phi}\frac{k}{\epsilon}(\overline{u_k' u_l'}\frac{\partial \overline{u_i'\phi'}}{\partial x_k} + \overline{u_k' u_i'}\frac{\partial \overline{u_l'\phi'}}{\partial x_k})] \tag{15}$$

where $c_{s\phi}$ is an empirical constant.

The only remaining term to be modeled in equation (11) is term (v), pressure-scalar correlation. From the arrangement of the terms of the equation, the pressure-scalar correlation is a counterbalancing term. Inside the term (iii), resulting in creation of $\overline{u_i'\phi'}$ because of the combined actions of the mean velocity and scalar gradients, the first and the second terms in this term tend to increase the velocity and scalar fluctuations, respectively [51, 57]. This general tendency to increase the creation of the $\overline{u_i'\phi'}$ by the production terms, i.e., the terms (iii) and (iv), may be balanced out when the pressure-scalar correlation term comes into effect [51, 57]. Hiring the Poisson equation for pressure fluctuations, the pressure-scalar correlation term can be written in form of three distinguished terms [51, 53, 57]

$$\frac{1}{\rho}\overline{p'\frac{\partial \phi'}{\partial x_i}} \equiv \pi_{i\phi} = \pi_{i\phi,1} + \pi_{i\phi,2} + \pi_{i\phi,3} \tag{16}$$

where $\pi_{i\phi,1}$ represents a pure turbulent interaction between the velocity and scalar fluctuations [53, 59]. To model the $\pi_{i\phi,1}$, equation proposed by Monin [60] is widely applied

$$\pi_{i\phi,1} = -c_{1\phi}\frac{\epsilon}{k}\overline{u_i'\phi'} \tag{17}$$

where $c_{1\phi}$ is a model constant. The second term in equation (16), $\pi_{i\phi,2}$, is responsible for the interaction between the scalar fluctuations and the mean velocity gradients [53]. Finally, the third term, $\pi_{i\phi,3}$ contributes to the effects of the body (gravitational) forces [59]. In analogy to the pressure- strain correlation term modeling, Launder [61] suggested that the quantities of $\pi_{i\phi,2}$ and $\pi_{i\phi,3}$ are correlated to the production of $\overline{u_i'\phi'}$ by mean strain and buoyancy, respectively.

$$\pi_{i\phi,2} = c_{2\phi}\overline{u_l'\phi'}\frac{\partial U_i}{\partial x_l} \tag{18}$$

$$\pi_{i\phi,3} = c_{3\phi}\beta g_i\overline{\phi'^2} \tag{19}$$

where $c_{2\phi}$ and $c_{3\phi}$ are the model constants.

With respect to the equations (11) to (19), there are several studies suggesting empirical constants of the models based on different experimental case studies to calibrate the model. For instance, as reported by Launder, there is a range of values that varies between 2.5 to 9.7 for $c_{1\phi}$ [57]. Table 1 shows the three sets of model constants for the scalar flux modeling equations suggested by Launder [61] and Gibson and Launder [62, 63], respectively.

Table 1 Constants of the SFM

Constants	$c_{1\phi}$	$c_{2\phi}$	$c_{3\phi}$	$c_{s\phi}$	c_{ϕ}	R	Ref
	3.2	0.5	0.5			0.8	[61]
	3.0	0.33	0.33	0.11	0.13	0.8	[62]
	3.0	0.5	0.5			0.8	[63]

Several constants participate in the set of the suggested equations for Reynolds flux modeling, and it becomes clear that the calibrating effects associated with theses constants is of importance for each case or application. However, numerical experiments for INBJs showed that, the introduced range for the constants in Table 1 is quite satisfactory, except for the $c_1\phi$. As discussed in the next subsection, $c_{1\phi}$ plays the major role in the equation (11) and can affect the mean concentration field. At the end of this section, it is worth emphasizing that equation (11) and its most important contributing terms for shear, buoyancy and redistribution of them, i.e., terms (iii), (iv), and (v) respectively, will be assessed to study how their correlation can predict the physics of INBJs.

2.2 Model constants and calibrations

Using the second-moment closure, SFM will be coupled with an RSM model. For the Reynolds stress modeling part, the SSG model ([64]) was used in this study. Launder [58] depicted conceptually how Reynolds stress, Reynolds flux, and turbulent fluctuations are interconnected to each other in horizontal and vertical buoyant turbulent shear flows. Figure 2 shows these multilateral connections. Indexes 1, 2, and the wavy lines represent the stream-wise direction, the direction of scalar gradients, and the pressure-scalar correlation, respectively. To accurately model an INBJ, it is necessary to consider the complex interconnectivity between its vertical and horizontal shear flows. Therefore, it is crucial to treat the calibration of the RSM and SFM models as a mutually coupled problem. In other words, in order to calibrate the numerical model, both the constants involved in the SFM and RSM (specifically, the SSG model in this case) models need to be considered for calibration. A similar procedure to the work of [22] is followed here. As mentioned in [22], two constants of C_1 in the SSG model and $c_{1\phi}$ in the SFM are of most importance in model calibration. For the sake of brevity, a thorough explanation is not included here and can be found in [22]. The set of the chosen constants to be implemented in the model for SFM in this study were as follows. $c_{1\phi} = 3.2$, $c_{2\phi} = 0.50$, $c_{3\phi} = 0.50$, $c_{s\phi} = 0.11$, $c_{phi} = 0.13$. These constants are defined within the implemented code for SFM inside the added piece of code augmented in the solver, which is pimpleFoam here, and thus, can be manipulated.

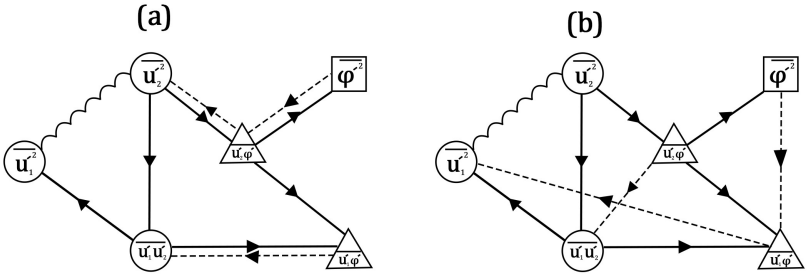

Fig. 2 Couplings of the Reynolds stress and Reynolds flux components in **(a)** horizontal and **(b)** vertical buoyant turbulent shear flows [56]

3 Case studies

Three turbulent 45° INBJs were simulated in this study. Table 2 shows the case studies and their related characteristics. Cases with the letter "H" in their ID refer to dense jets with high density differences, while the case SFM-L1, with the letter "L", refers to a lighter jet, compared to the other cases. More details on the range of the hired Fr and the density differences are discussed under "Results and discussion" section, later. The density difference in the solver can be applied through the defined fields for the scalar being transported. In this regard, the two fields, density and concentration, can be defined and the inlet and internal fields would represent the jet and receiving ambient characteristics, respectively. In other words, equation (6) relates the density to the concentration (i.e., equation (4)) and then the updated density field is included in the solver through the last term in equation (3). Given that the flow is symmetrical with respect to the vertical symmetry plane across the nozzle, a symmetric tank with $1.8Fr_dD$ width, $6Fr_dD$ length, and $2Fr_dD$ height for the largest Fr number was created with a nozzle diameter of $6mm$. Dimensions of length, width, and height were chosen based on the criteria practiced by Zhang et al. [44]. Nozzle tap (at elevation H_0 in Fig. 1) was placed above the bottom based on the findings of Crowe [21] ($\frac{H_0}{FrD} \geq 0.6$) to avoid any boundary influence. The Computational domain was discretized using hexahedral elements. Grids density was reinforced around the nozzle in the longitudinal, upward vertical and spanwise directions. Figure 3 shows an isometric view besides the grid distribution pattern on the central symmetrical plane. A boundary condition of the free slip type was applied to the top, while a zero gradient boundary condition was used for the other sides, except for the back and bottom which were assigned with wall boundary condition. The nozzle was set as an inlet with known discharge velocity at a turbulence intensity of 5%. Concentration variation along the centerline on the centerline peak and the return point were monitored to check for the mesh independence. Grid refining was continued till the return point dilution did not change more than 2%, compared to the mesh created before. The final geometry contained 955060 elements. For temporal discretization Crank–Nicolson scheme was used. Divergence and Laplacian

terms were discretized using second-order TVD (total variation diminishing) limited linear and central difference (linear), respectively. Implementation of the SFM along with the modifications (e.g., the buoyancy production terms augmentation) required for the momentum flux modeling (i.e., the turbulence model) were conducted in OpenFOAM v6 [65]. To include the SFM, a piece of code (.H) containing all the coded Reynolds flux model equation ((11)) was added into the solver (pimpleFoam), while solving a transport equation of the concentration (equation (4)), and the turbulence model (i.e., the SSG model) was modified to represent the turbulent buoyancy generation/destruction. Concerning the execution time of the simulations, for the case SFM-L1, the cLocktime of the simulation was 84172 seconds ($\sim$ 24 hrs) with six processor involved from Compute Canada (Canada's national high-performance compute (HPC) system), while clocktime of run SFM-H1 is nearly 50% higher for the same number of processors on this supercomputer processors on HPC. Simulations were performed on different nodes on Cedar cluster with CPU-based Intel Platinum 8160F Skylake @ 2.1Ghz (More information can be found here [1]).

Table 2 Initial conditions for simulations within different scenarios

Case ID	Velocity ($\frac{m}{s}$)	Brine density ($\frac{kg}{m^3}$)	$\frac{\Delta\rho_0}{\rho_a}$(%)	Fr	Re
SFM-H3	0.483	1034	3.50	10	3269
SFM-H1	0.670	1028	3.00	15	4536
SFM-L1	0.516	1009	1.00	20	3493

4 Results and discussion

4.1 Trajectory and bulk parameters

Figure 4 depicts the non-dimensional concentration ($\frac{C}{C_0}$) field of case SFM-H1 with $Fr = 15$. Counters of non-dimensional concentration are also added in the figure. As seen, at a very short distance from the nozzle, the jet is already reached half of its initial concentration at the origin. The distance needed for the jet to be diluted by a factor of two or more on its centerline is much shorter when the jet is in the jet-like region, compared to the plume-like region where the flow is descending. This comes more clearly by taking the contours of 0.50, 0.25 and 0.1 of concentration ratio, C/C_0 in Fig. 4. As seen, the distance between the contours of 0.5 and $0,25$ on the centerline in the jet-like region is much shorter than the distance it takes to get from the contour of 0.1 to the contour of 0.05 (on the centerline). This can be seen as an indicator of the contribution of each phase of jet-like and plume-like regions to the mixing process.

[1] https://docs.alliancecan.ca/wiki/Cedar

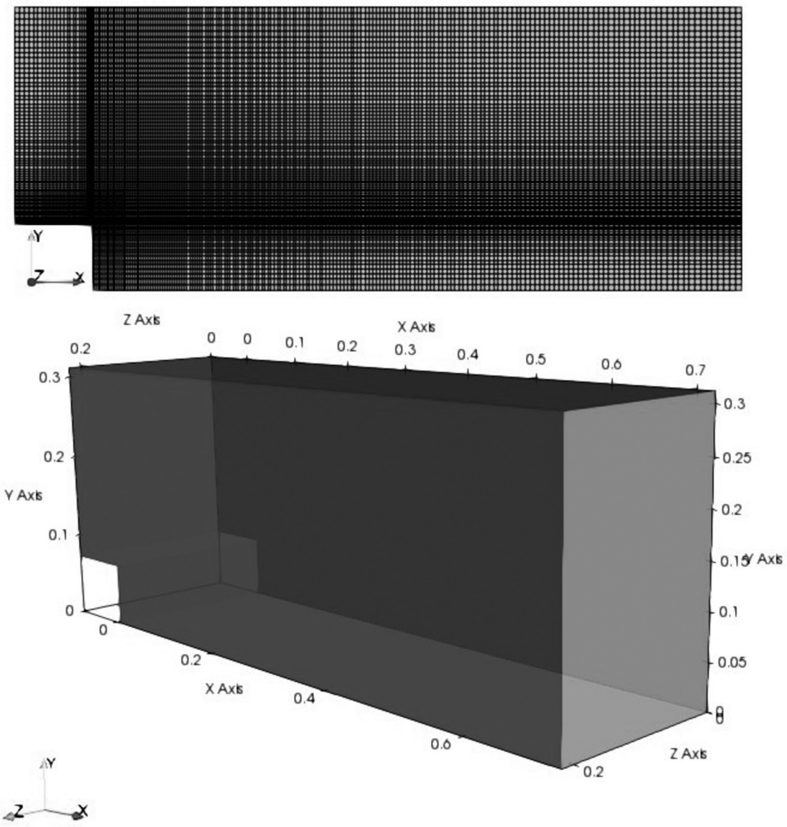

Fig. 3 Isometric view and symmetry plane of the computational domain

Figure 5 shows the maximum concentration and velocity decay along the centerline of the jet, respectively. As seen, both concentration and velocity constantly decrease. However, the tendency to decrease is much greater before the jet centerline is reached (indicated by horizontal distance X_m), compared to descending phase of the jet. Slopes for both graphs are milder when the jet is in its plume-like region implying that the mixing process on the centerline gets slower when it is far from the nozzle. It also can be noticed from Fig. 5 **(a)** that the jet lost up to 80% of the initial concentration before the jet reached the centerline peak. For the velocity field, Fig. 5 **(b)**, the situation is even more noticeable, where the maximum centerline velocity dropped to about 10% of its initial counterpart around the X_m. Compared to the experimental data, the agreement with the data is very well, except for the tail of the velocity decay where the slope is much milder than the data. This can partially be attributed to the fact that the distances here are not dimensionless using Fr. As a result, it is difficult to distinguish whether the jet is in exact accordance with the data, specifically after the jet meets the return point and impinges the bottom and continues as a density current.

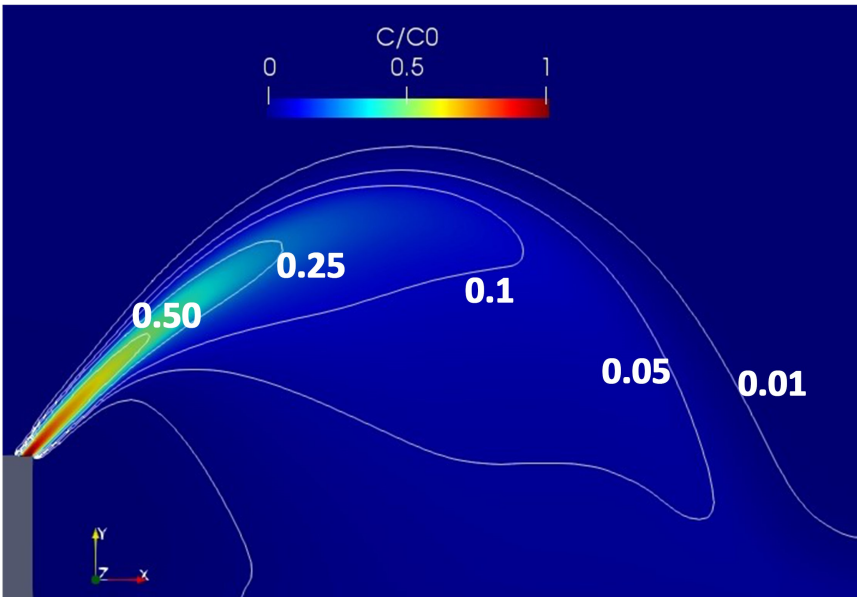

Fig. 4 Non-dimensional concentration field of case SFM-H1 with $Fr = 15$ on the symmetry plane

As expected, a more meaningful consistency with data may be seen when they are represented in dimensionless form using densimetric Froude number. Figure 6 shows the centerline velocity decay for each component. From the figure, the agreement with the data of [21] is very good for both components, compared to the Fig. 5. It is also of interest to see that the decay rate of the horizontal component is gentler than that of the vertical component. This is the case specifically before the centerline peak is reached and the jet is still ascending. After that point, both graphs flattened due to a less contribution of the descending phase to the mixing process. The more rigorous slope of decay of the vertical velocity component may be perceived in terms of the conflict of the upward direction of the momentum with gravitational force in the opposite direction.

Trajectories of the simulations are plotted against each other and some LES, RANS, and experimental data for comparison in Fig. 7. From the figure, some insights to the numerical results are perceivable. Three groups falling together are discernible. One group can be seen as RANS modeling with low Froude numbers. This is the case for $Fr = 10$ from the present study (case SFM-H3) and $k - \epsilon$ from the study conducted by Zhang et al. [45]. Although the case with $Fr = 35$ simulated using $k - \epsilon$ also shows a huge diffusive performance, cases with $Fr = 10$ show retrieving trajectories regardless of the turbulence modeling approaches used. This is justified by looking into the literature where it is discussed that the densimteric Froude number ranges have certain effects on the mixing and geometric of INBJs (e.g., [66], [10], [42]). Roberts and Toms [66] suggested a value of $Fr = 25$ to cancel out any effects

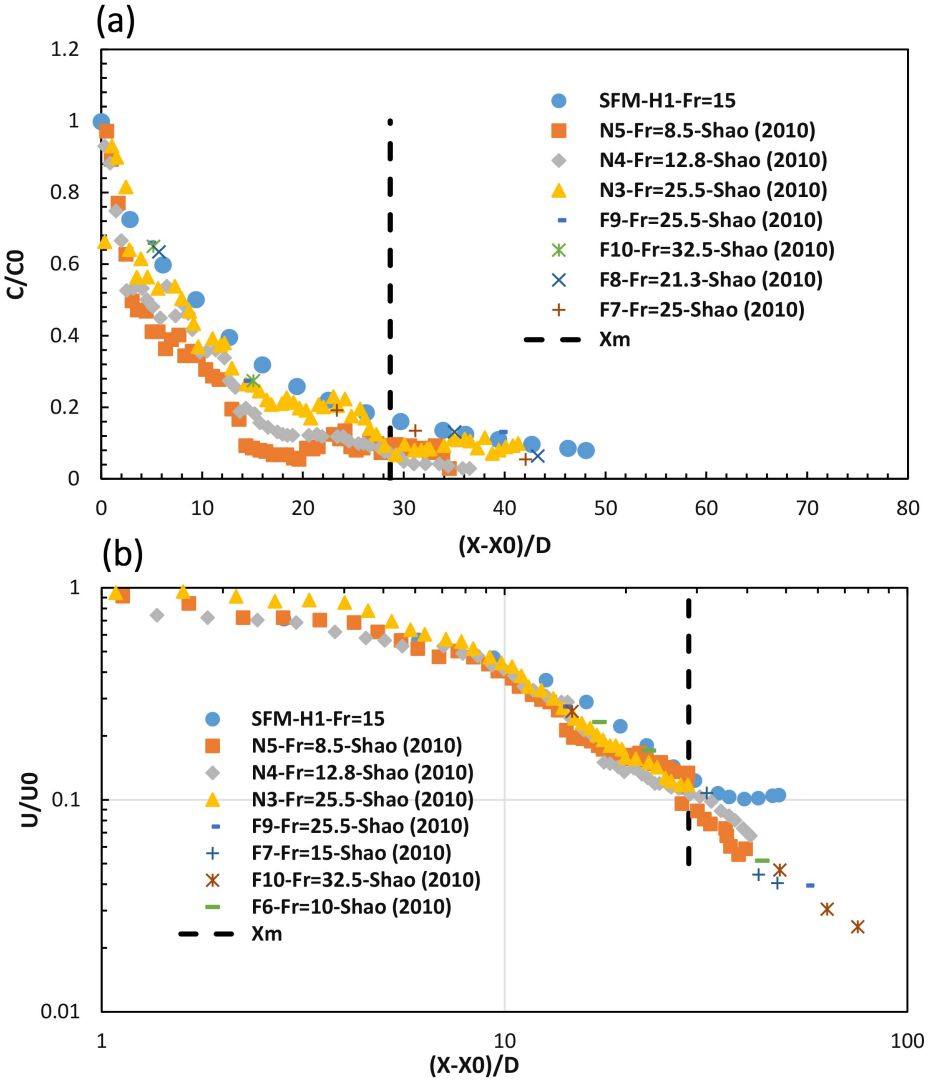

Fig. 5 Maximum **(a)** concentration and **(b)** velocity decay along the jet centerline

associated with the volumetric flux. Based on the results of Lai and Lee [10], dimensionless dilution ratios at the return point may fall onto a constant for $Fr > 20$. Moreover, they noted that the dimensionless terminal rise height has an additional dependence on the Froude number for small Fr and approaches close to a constant when $Fr \geq 25$. However, interestingly, LES simulation with $Fr = 10$ from the Zhang et al. [44] contradicts this conclusion, where the difference between that and the case with $Fr = 14.9$ is not much noticeable. The results for the case with $Fr = 10$ from the present simulation and the case from [44] with the same Froude number show that SFM is much less

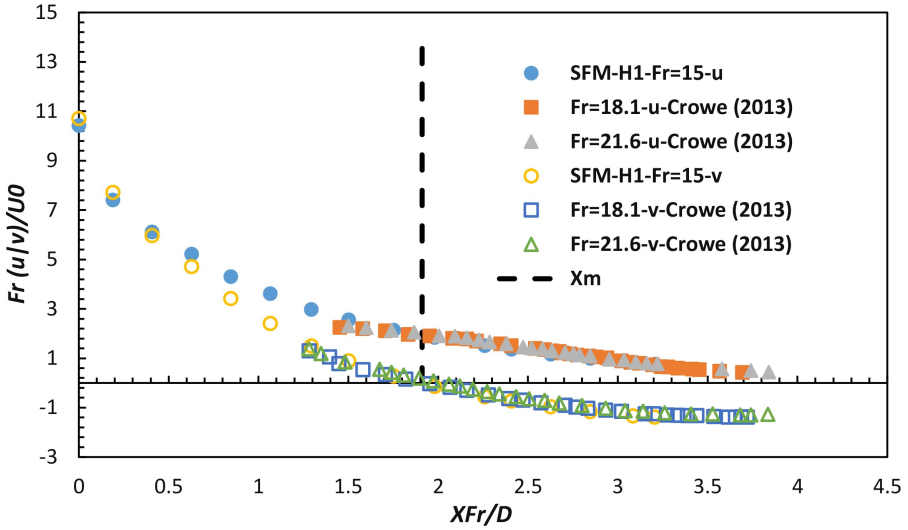

Fig. 6 Components of centerline velocity in comparison with experimental data

diffusive than the standard $k-\epsilon$ model. Another reason for the differences here could be attributed to the fact that the case SFM-H3 not only has the least Froude number but also the highest density difference, $\frac{\Delta\rho_0}{\rho_a}(\%) = 3.5$, among the others. Density differences and the Froude numbers, in the present study, were deliberately chosen to be lower than or equal 20 to prevent collapsing into any Froude number-independent pattern observed in cases with high initial momentum. Such high densimetric Froude numbers may cancel out any other important effects due to the dominance of the initial momentum.

Another discernible group, which can be seen in Fig. 7, represents those with a tendency to overpredict the experiments. These are, mainly, LES cases where, in accordance with almost all other LES studies in the literature, geometrical parameters of the INBJs have been predicted very well using this approach. This has been the case even with those simulations with a considerable grid number differences (e.g., [49] used much fewer grid numbers than [46]).

The third group refers to those in between, where a very reasonable agreement between the experimental data and the numerical is observable. Cases with $Fr = 15$ and $Fr = 20$ from the present study using SFM show that the Reynolds flux modeling is capable of reproducing the geometrical features of the INBJs very well. This has been reported before for a larger Froude number ($Fr = 25$) in the study of [22].

Jet growth or spread, which can be defined as the radial distance from the centerline to the point in which the concentration or velocity is decreased to $\frac{1}{e}$ of their centerline counterparts, is another insightful feature of the dense jets (Fig. 8). Jet growth can be investigated either in form of the mentioned definition or the dimensionless cross-sectional distribution of concentration and

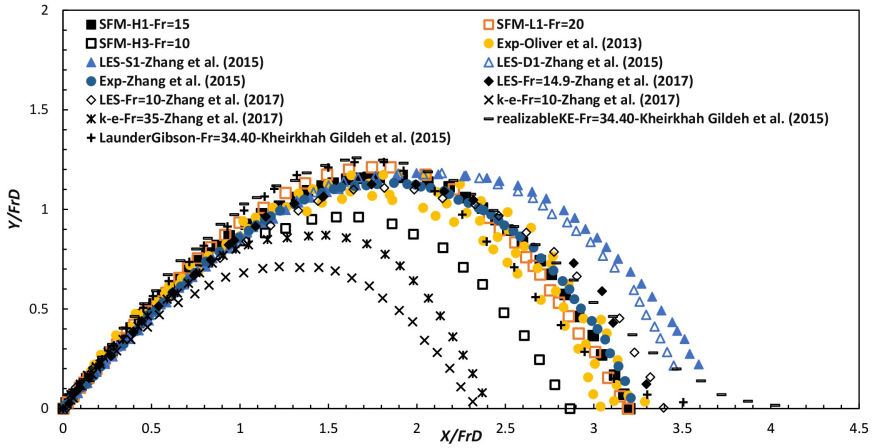

Fig. 7 Trajectories extracted for the present case studies alongside the LES, RANS, and experimental data

velocity in different locations of the jet flow. Here, the jet growth is depicted in form of lower and upper $\frac{1}{e}$ concentration (b_c) and plotted against the distance from the nozzle on the centerline. As seen, the scatter of the data is noticeable. An important point about the result reported from the study of Zhang et al. [44] is that they used 5% of the centerline concentration for the b_c definition. However, the differences between the results is still considerable given that it is expected to see higher values for lower b_c using the 5% definition instead of $\frac{1}{e}(\sim 37\%)$. Comparing the result with the data from the LES and experimental data by Jiang et al. [46], it turns out that the lower b_c is overpredicted. This can be attributed to both the SFM and RSM models. However, as a general issue with RSM models, it has been reported before in the literature that the jet spread rate overprediction is well known with these models [67]. Regarding the resemblance of the nature of the SFM and RSM, the same argument may be applied. However, the interaction of the turbulent flux and momentum may be seen as a factor that can intensify the overprediction observed here and is worth further investigation. When comparing the inner and outer b_c, one may notice that the latter is more prone to agree with the data than its counterpart. This is due to the detrainment process which occurs in the inner side of the flow. In other words, the inner side of the flow is under the effects of the buoyancy forces and unstable density gradients, while the outer layer is governed by the stable density gradients resisting the mixing. The main drawback with the SFM, here, is that it is not capable of capturing the detrainment process in terms of the buoyancy-induced instabilities by convective mixing. One source of improvement, among others, might be found in calibration of the participating constants which needs to be studied more comprehensively. A qualitative comparison for the inner b_c can be seen in Table 3 where the result of the present study is closer to experimental data of Shao and Law [9].

The report of Papakonstantis et al. [7, 8] shows a better agreement with the LES data of Zhang et al. [44].

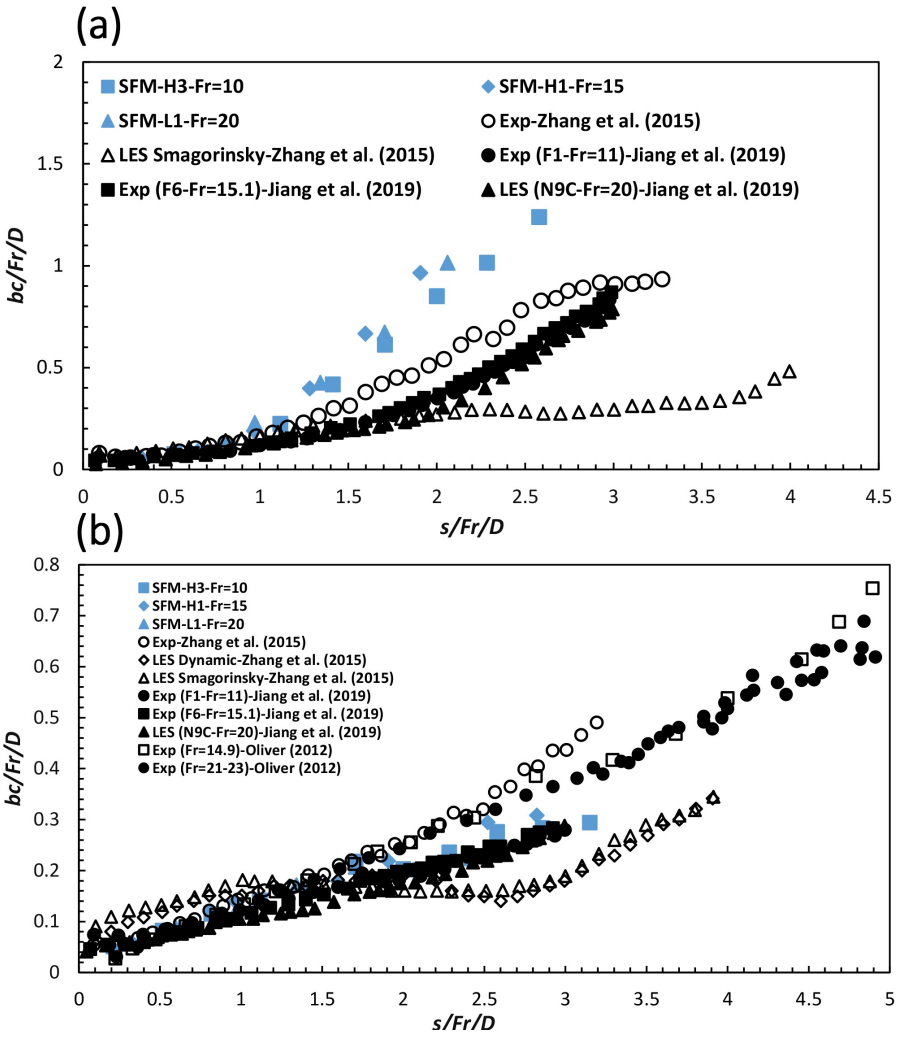

Fig. 8 Variation of jet growth rate, b_c, for the **(a)** inner and **(b)** outer layer of the flow

To complete the bulk parameters assessments, six important trajectory and mixing parameters are compared in Table 3. From the table, it can be seen that except for the case SFM-H3 with $Fr = 10$, the agreement of the data is very good with previous studies. Values in parenthesis refer to an absolute error with regard to the average of the reported experimental data. Positive and negative signs are used to point to over and under predictions, respectively. Regarding the mixing parameters at the centerline peak, S_m/Fr, and

the return point, S_r/Fr, both are in agreement with the experiments, compared to the LES results. Regarding the results of [44], and [45], the present study shows an 11% improvement over their results. As it was mentioned earlier, the mean concentration field and mixing have been more challenging to predict than the geometrical characteristics using different numerical approaches. SFM approach is capable of addressing the mixing parameters prediction very well due to the set of complex interactions between the different turbulence contributors of the flow involved in the model, compared to other simple approaches (specifically the widely used SGDH approach) where it only has the gradient of the scalar field to be related to the turbulence as is in the Boussinesq analogy.

Table 3 Summarized comparison of dimensionless geometrical and mixing parameters with the last column on the inner jet growth (b_c)

Quantities	$\frac{X_m}{DFr}$	$\frac{Y_m}{DFr}$	$\frac{Y_t}{DFr}$	$\frac{X_r}{DFr}$	$\frac{S_m}{Fr}$	$\frac{S_r}{Fr}$	$\frac{b_c}{DFr}$
SFM-Present study							
SFM-H3-Fr=10	1.67	0.94	1.33	2.82	0.43	1.01	0.85
	(-11%)	(-20%)	(-19%)	(-9%)	(-5%)	(-0.22%)	
SFM-H1-Fr=15	1.91	1.15	1.54	3.20	0.46	1.20	1.28
	(+2%)	(+1%)	(-2%)	(+4%)	(+2%)	(-8%)	1.28
SFM-L1-Fr=20	1.89	1.20	1.51	3.19	0.50	1.21	1.18
	(+1%)	(+5%)	(-4%)	(+3%)	(+10%)	(-7%)	1.18
Num-Zhang et al. [44]							
LES	2.06	1.26	1.46	3.71	0.26	1.06	0.3
Num-Zhang et al. [45]							
LES	1.97	1.13	1.35	3.32	0.32	1.00	
standard k-ϵ (wall function)	1.38	0.72	1.04	2.45	0.45	0.74	
standard k-ϵ (near-wall modeling)	1.30	0.74	1.06	2.38	0.44	0.71	
Exp-Cipollina et al. [5]	1.80	1.17	1.61	2.82	-	-	
Exp-Kikkert et al. [6]	1.84	1.06	1.60	3.26	-	-	
Exp-Shao & Law [9]	1.69	1.14	1.47	2.83	0.46	1.26	0.78
Exp-Papakonstantis [7, 8]	2.03	1.17	1.58	3.16	0.52	1.55	0.28
Exp-Lai & Lee [10]	2.09	1.19	1.58	3.34	0.45	1.09	
Exp-Oliver et al. [11]	1.75	1.09	1.65	3.13	0.39	1.22	
Exp-Jiang et al. [47]							
Fr=21	-	-	1.52	3.03	0.46	1.37	
Fr=26	-	-	1.61	3.17	0.44	1.33	

4.2 Turbulence parameters

The main turbulence characteristic that is discussed here is the turbulent flux vector (i.e., the Reynolds flux modeled using the second-moment closure. Figure 9 shows the velocity and Reynolds flux vectors in a non-scaled format. Such demonstration helps capture the behavior of the flow regardless of the magnitude of vectors (which is discussed later). Based on the velocity vector map distribution, the entrainment of the ambient flow to the core of the jet flow is evident. It is highlighted on Fig. 9**(a)** with dashed lines. The entrianment happens all over the top of the flow in the outer layer. This is the main cause of the mixing. When the ambient water is sucked into the core of the jet flow, turbulence, by shear, is generated.

As can be seen from the distribution of the turbulent fluxes, there is a tendency in the vectors to move outwards. As was declared in the study of Shao and Law [68] for horizontal offset jets, vectors of turbulent fluxes move from the regions with higher concentration (e.g., the centerline) to the regions with lower concentration (e.g., the ambient). There are more analogies with the experimental report of [68]. For instance, It can be seen that the direction of the vector fluxes is a function of the inclination itself. For a horizontal dense jet, the jet is immediately tilted down, and thus, two downward and upward groups of Reynolds flux represent lower and upper shear layers of the flow, respectively. However, for a 45° inclined dense jet, the inclination results in two upward and almost horizontal group of vectors escaping the high concentration areas. Another analogy with the experimental data is where the flow is in its descending phase. As seen in Fig. 9**(b)**, vectors of turbulent flux move across the jet from the inner layer to the outer layer. This is consistent with the upward movement of the turbulent fluxes in the transition to wall-jet phase of horizontal offset jets in [68]. The complex behavior of the Reynolds fluxes captured by the SFM, i.e., using the equation (11), is in contrast with a simple Boussinesq-based model as SGDH.

Figure 10 shows the the map of the Reynolds flux with the size of the arrows in proportion with the magnitude of the vectors. From the figure, it can be seen that the main escape of the vectors from the core of the flow to the ambient happens right after the unmixed gap of the flow off the nozzle and is marked with a close shaped on the figure. This unmixed gap was noted by the Shao and Law [68].

Figure 10 shows that the two upper and lower shear layers contribute to the mixing before the centerline peak is reached and in the middle of the jet-like region. This is consistent with the fact that the flow is reached up to the 50% of its initial concentration in a short distance from the nozzle (Fig. 4). Figure 10 also reveals that the outer layer has more contribution in turbulence generation than the inner layer. This can be related to the observation of Oliver et al. [11] where they attributed the more fluctuated outer layer of the flow to the more resistance of the stable density gradients to the mixing.

Figures 11 and 12 show comparisons between the horizontal, $\overline{u'c'}$, and vertical, $\overline{v'c'}$ components of the turbulent mass flux for a case simulated with

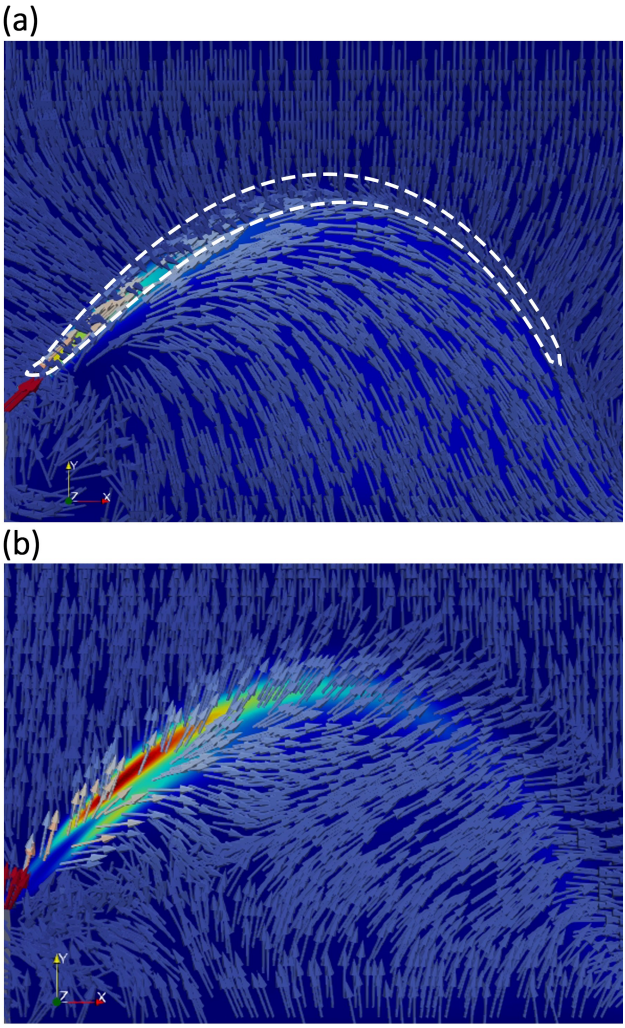

Fig. 9 Non-scaled vector map of the **(a)** velocity and **(b)** Reynolds flux. Zone of entrainemnt on the symmtery plane is higlighted with the dashed line

SGDH and SFM at jet-like, centerline peak and plume-like regions, respectively. The results taken from each approach are shown separately in Fig. 11 for a better comparison in the jet-like region. One should note that in Fig. 11-16 the negative values of r/b_c imply the outer layer of the flow while the positive ones represent the inner layer of the flow. The turbulence model used for the case shown in the Fig.11**(b)** to model the Reynolds stress tensor was realizable $k-\epsilon$ so that the simulation was conducted using fully Boussinesq-based modeling. Realizable $k-\epsilon$ was previously reported as the best EVM model in CFD simulations of INBJs [41].

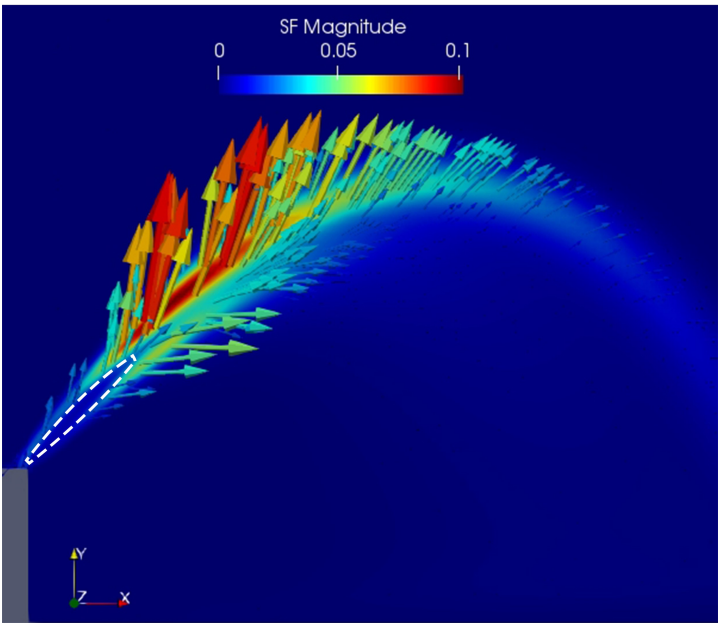

Fig. 10 Vector map of the Reynolds flux with the size of arrays proportional to the magnitude of turbulent vector fluxes of concentration. The dashed closed shape marks the unmixed gap

From the figure, it can be seen how SFM and SGDH model the turbulent mass flux, differently. This is the case for the vertical component, $\overline{v'c'}$, in the inner layer and the horizontal component in the outer layer. SGDH results imply that the mass flux vector in the outer layer is moving in the opposite direction of the flow with respect to the negative and positive values for horizontal and vertical components in this region, respectively. These directions make turbulent flux vectors move backward which is a non-physical implication of the method. Figure. 10 shows that, for instance, in the outer layer, although being tilted up from the centerline, vectors move alongside the flow direction. Differences counted for the jet-like region apply to the centerline peak and the plume-like region as well. From Fig. 12**(a)**, both methods show a similar peak value for the $\overline{v'c'}$ at the outer layer while the differences are noticeable in the inner layer. For the plume-like region in Fig. 12**(b)**, on the contrary, SGDH shows a huge increase for the vertical component in the outer layer. With regard to the lower shear forces expected to be seen in the plume-like region, in comparison with the jet-like region, it may be concluded that the performance of SGDH is, again, non-physical, compared to the SFM.

As mentioned before, concentration fluctuation, $\overline{\phi'^2}$ (or $\overline{c'^2}$ in our case) is the counterpart of the turbulent kinetic energy for the scalar field. Thus, it can be seen as an indicator of the intensity of turbulence for the scalar. Figure 13 shows the evolution of the turbulent kinetic energy and concentration fluctuation in three sections in the middle of the jet-like region, the centerline

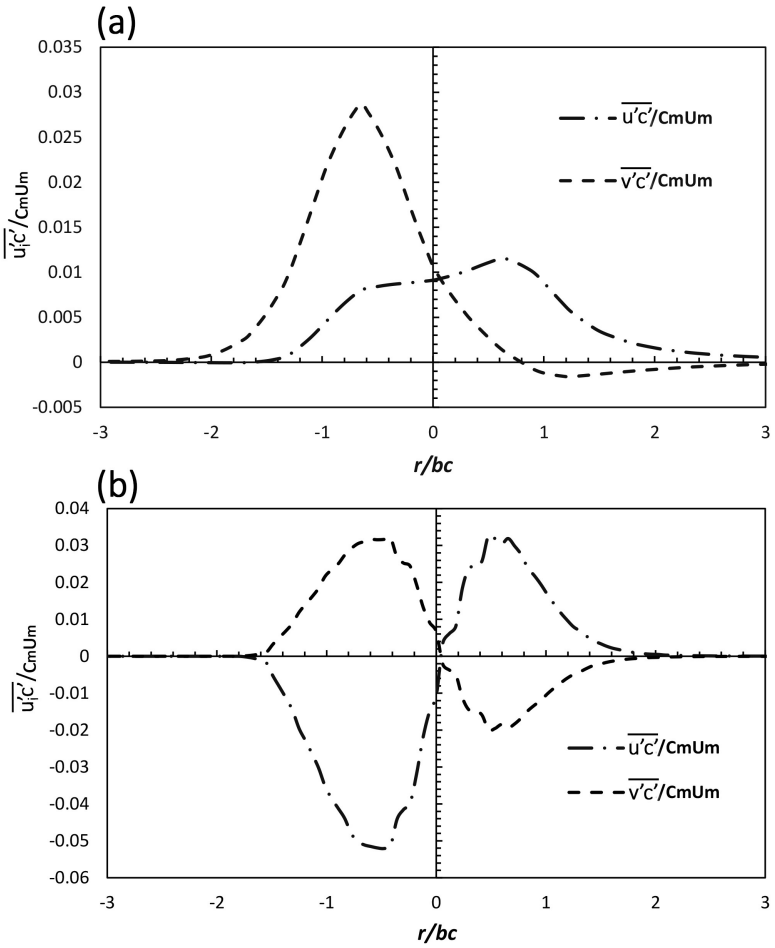

Fig. 11 Horizontal and vertical components of the turbulent mass flux in **(a)** SFM and **(b)** SGDH simulations in the middle of the jet-like regions

peak, and the middle of the plume-like region, respectively. It should be noted that c' here is, in fact, $\sqrt{\overline{c'^2}}$ and the form of depiction is for simplicity. As can be seen from the figure, there is an increase in the peak values that happens in the outer layer moving from the jet-like region to the plume-like region. This could be attributed to the fact that the outer layer resists the mixing due to stabilizing density gradients in these regions. This resistance, however, in the plume-like region is more evident due to the decrease in the initial momentum at the nozzle tap. A comparison with the experimental data at the centerline peak is provided in Fig. 14, where the consistency of the present results with the experimental data from Papakonstantis et al. [8] is evident. Regarding the report of Oliver et al. [11] and Lai and Lee [10], results are overpredicting the inner side of the flow.

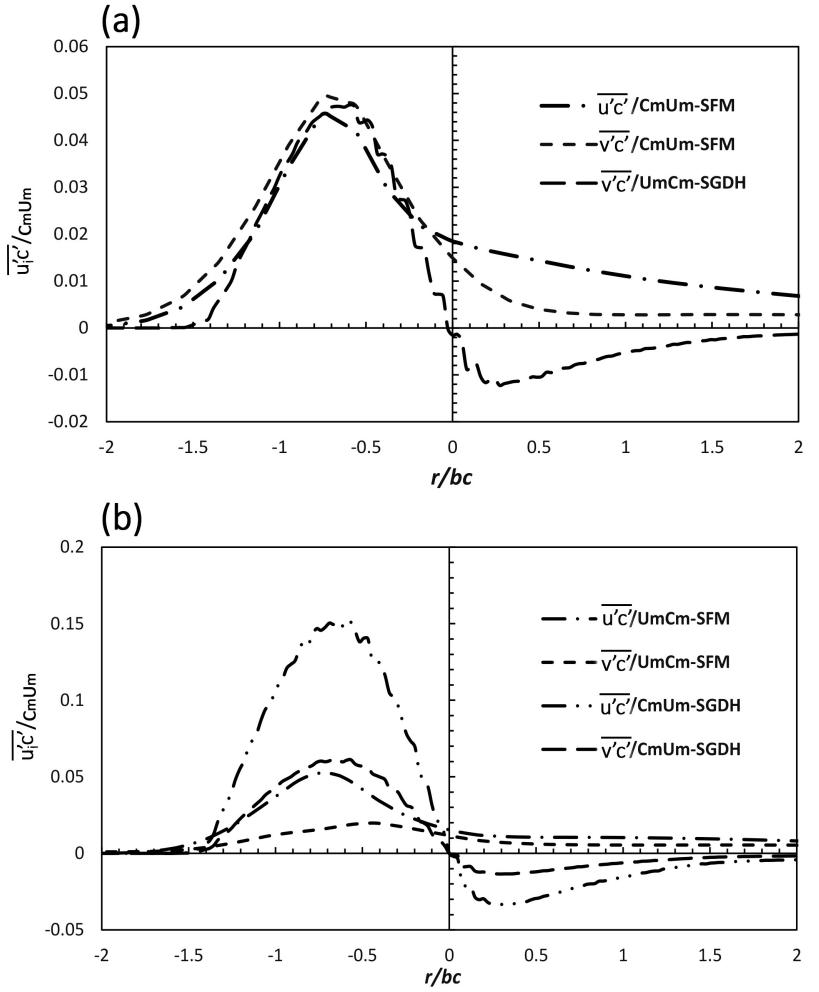

Fig. 12 Horizontal and vertical components of the turbulent mass flux in **(a)** centerline peak and **(b)** plume-like regions

As shown before, concentration fluctuation participates in the SFM equation (i.e., equation (11)) in the buoyancy production term. There are other terms participating in the model and are assessed in the following. With regard to the fact that the effects of spatial diffusion and the viscus destruction are negligible, three important terms in equation (11) can be counted as production due to shear, turbulence production due to the buoyancy, and the pressure-scalar correlation. These terms are tabulated in Table 4. As can be seen from the table, the rapid back to isotropy term contains the gradient of velocity and is responsible to prevent the fluxes to increase rapidly due to the imposed sudden changes in strain rate, while the slow back to isoptopy term is mostly responsible for the turbulent-turbulent interactions in absence of any

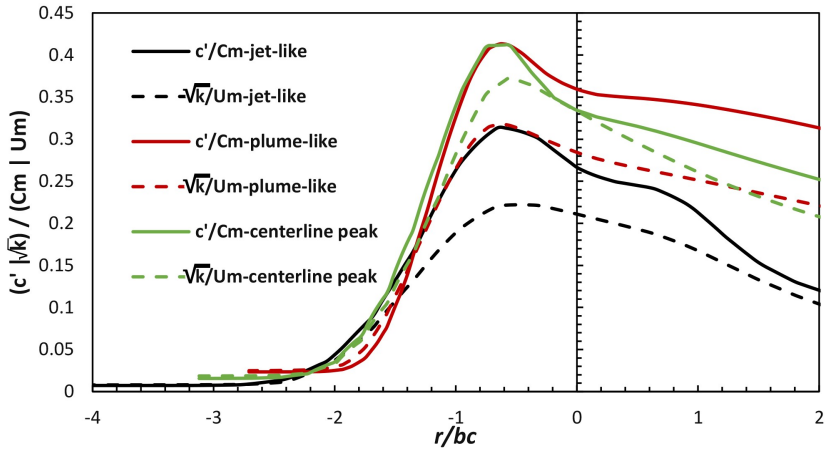

Fig. 13 distribution of turbulent kinetic energy and concentration fluctuation over three sections from upstream to the downstream of the flow

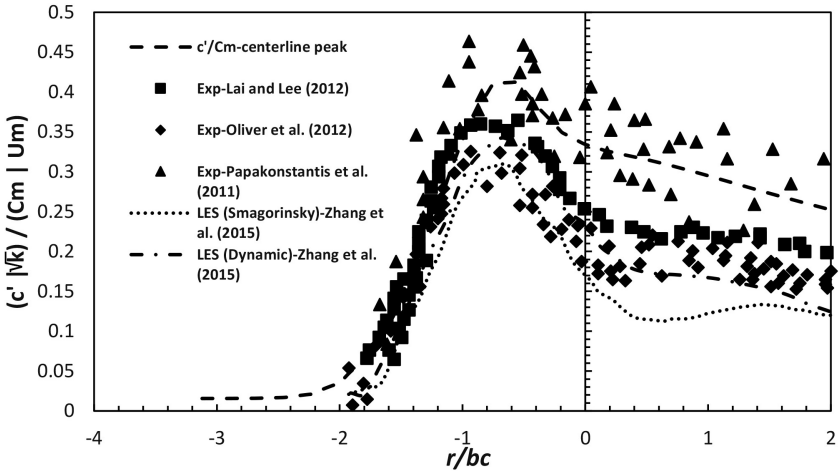

Fig. 14 distribution of concentration fluctuation at the centerline peak in comparison with the literature

gradient from the mean-field and tends to decrease the increase of turbulent fluxes, slowly [56].

Regarding the production of turbulence being carried into the flow due to the shear and buoyancy forces, these turbulence generator terms are plotted next to each other in the middle of the jet-like and plum-like regions and shown in the Fig. 15**(a)** and Fig. 15**(b)**, respectively. From the figure, some interesting insights into the turbulence characteristics are perceivable. Contribution of buoyancy and shear to the turbulence generation significantly change moving from the jet-like to the plume-like region. However, similar to the concentration fluctuation profiles, peak values happen at the outer layer. Regarding

Table 4 Participating terms in equation (11)

SFM components	Physical implication
$-[\overline{u_i' u_j'} \frac{\partial \Phi}{\partial x_j} + \overline{u_j' \phi'} \frac{\partial U_i}{\partial x_j}]$	Shear production
$-\beta g_i \overline{\phi'^2}$	Buoyancy production
$\frac{1}{\rho} \overline{p' \frac{\partial \phi'}{\partial x_i}}$	Pressure-scalar correlation:
$\pi_{i\phi,1} = -c_{1\phi} \frac{\epsilon}{k} \overline{u_i' \phi'}$	Slow back to isotropy
$\pi_{i\phi,2} = c_{2\phi} \overline{u_l' \phi'} \frac{\partial U_i}{\partial x_l}$	Rapid back to isotropy
$\pi_{i\phi,3} = c_{3\phi} \beta g_i \overline{\phi'^2}$	Buoyancy generation redistribution

the turbulence generation due to the buoyancy, G, the contribution of the buoyancy experiences an increased share, compared to the shear production, when moving from the jet-like to the plume-like region. The increased share of the buoyancy to the turbulence in the plume-like region can be attributed to the fact that the detrainment process that takes place here is much more than that for the jet-like region, which is a buoyancy-driven tendency of the denser flow to go downward. Buoyancy generation in the SFM equation (i.e., equation (11)), is, proportional to the concentration fluctuation. As a result, it is expected to see that it decays moving from the outer layer towards the inner layer, which is evident in the figure.

Concerning the shear production and both directions of horizontal and vertical involved, the vertical component, P_y, has more contribution in the jet-like region than the horizontal one, P_x, compared to the plume-like region where the situation is reversed. The higher values of the vertical component in the jet-like region can be seen in accordance with the tendency of the turbulent scalar fluxes to move from high-concentration regions to the regions with lower concentration, which occurs, with the most intensity, in the middle of the jet-like region (Fig. 10). On the other hand, when in the plume-like region, the dominance is with the horizontal component. In this region, fluxes are more intended to move horizontally than vertically, because a horizontal departure to move to a low-concentration region is less-energy demanding. However, when in the jet-like region, turbulent scalar fluxes have to move upward to move towards a low-concentration area where they confront the resistance of the stable density gradients resulting in a very high-turbulent region (Fig. 10).

It is also worth mentioning that, as a general comparison, the contribution of buoyancy was less important, compared to the shear forces and the peak values of the turbulence generations occur in the outer layer. The lower importance of the turbulent buoyancy generation in negative buoyant jets has been previously reported by Cresswell and Szczepura [69], where they reported on the balance of the terms involved in the turbulent kinetic energy and the momentum equation finding the main contribution of the buoyancy from the mean motion (i.e., the momentum equation), compared to the turbulent kinetic energy. The importance of the different terms and their physical implications shown for INBJs can lead to model simplifications for these types of flow in

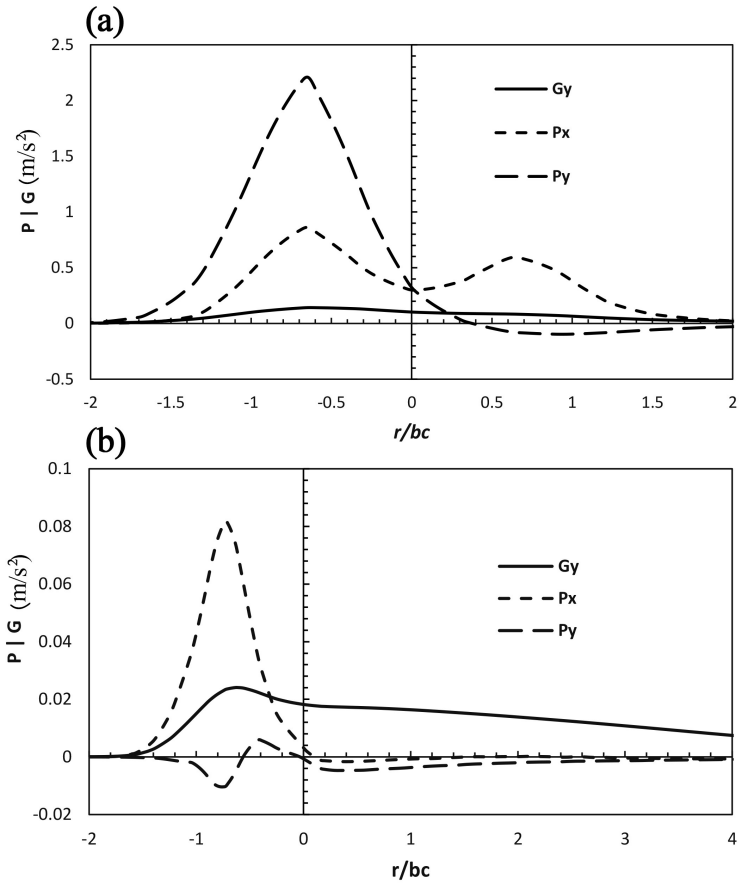

Fig. 15 Turbulence production due to the shear (P) and buoyancy (G) at the middle of **(a)** jet-like and **(b)** plume-like regions

terms of an implicit second-order transport equation for the Reynolds flux, which will be discussed in another study.

Redistribution role of the pressure-scalar correlation can be seen in Fig. 16. As seen, components of the pressure-scalar correlation counter balance the distributions due to the shear and buoyancy proportional to their values, compared to Fig. 15. Since back to isotropy for the shear terms consists of slow and rapid parts, the overall value is represented here. Regarding the bigger share of the shear in comparison with the buoyancy discussed earlier, the pressure-scalar correlation for rapid and slow back to isotropy also provides a larger contribution when compared to the redistribution due to the buoyancy.

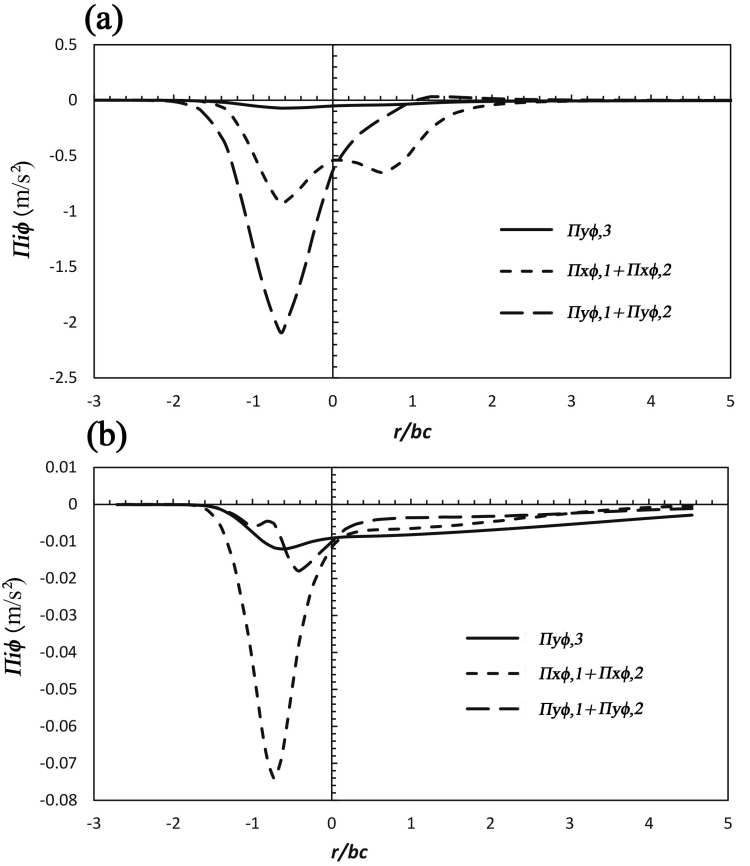

Fig. 16 Pressure-scalar correlation and its components at the middle of **(a)** jet-like and **(b)** plume-like regions

5 Conclusion

Simulations of 45° inclined dense jets were conducted using scalar flux modeling (SFM). Here are the most important concluding remarks on this study.

• SFM is capable of predicting both geometrical and mixing parameters in good agreement with the experimental data. Except for one case (i.e., case SFM-H3 with the highest density difference and the lowest Fr), none of the bulk parameters were predicted with more than 10% absolute error, compared to the average of experimental data.

• It was shown that the turbulent scalar vector, $\overline{u'\phi'}$, predicted using SFM is much more consistent with the physics of the INBJs, compared with the SGDH.

• Participating terms in the SFM equation were extracted and contrasted along side each other to see the contribution of each turbulence generation

processes of shear and buoyancy in the jet-like and plume-like regions of the flow. Share of buoyancy and shear to the turbulence generation significantly change moving from the jet-like to the plume-like region.

• It was observable that the contribution of the shear is more significant than the buoyancy, which was previously reported in the literature for the jets with negative buoyancy.

• The importance of the different terms and their physical implications shown for INBJs can lead to model simplifications for these types of flow in terms of an implicit second-order transport equation for the Reynolds flux, which will be discussed in a subsequent study.

6 Acknowledgments

This research was enabled in part by support provided by WestGrid (www.westgrid.ca) and Compute Canada Calcul Canada (www.computecanada.ca).

7 Statements and Declarations

• **Conflict of interest** The authors declare that they have no known competing financial interests or personal relationships that could have appeared to influence the work reported in this paper.

• **Author contributions** All authors whose names appear on the submission made substantial contributions to the conception or design of the work.

• **Funding** The authors have no relevant financial or non-financial interests to disclose.

• **Data availability** The datasets generated during and/or analyzed during the current study are available from the corresponding author on reasonable request.

8 List of symbols

$\mathbf{b_{ij}}$ Reynolds stress anisotropy, $\mathbf{D}$ nozzle diameter, $\mathbf{Fr}$ densimetric Froude number, $\mathbf{G}/\mathbf{G_{ij}}$ buoyancy production, $\mathbf{g}$ gravitational acceleration, $\mathbf{k}$ turbulent kinetic energy, $\mathbf{P}/\mathbf{P_{ij}}$ pressure/stress production, $\mathbf{R}$ ratio of dynamic to scalar time scales, $\mathbf{S}$ salinity, $\mathbf{Sc_t}$ turbulent Schmidt number, $\mathbf{S_m}$ centerline peak dilution ratio, $\mathbf{S_r}$ return point dilution ratio, $\overline{\mathbf{S}}_{\mathbf{ij}}$ mean strain rate, $\mathbf{S}_\phi$ source term, $\mathbf{t}$ time, $\mathbf{U_0}$ initial jet velocity, $\overline{\mathbf{u_i'u_j'}}$ Reynolds stress tensor, $\overline{\mathbf{u_i'}\phi'}$ Reynolds flux vector, $\overline{\mathbf{W_{ij}}}$ mean rate of rotation tensor, $\mathbf{X_m}$ horizontal distance of the centerline peak to the origin, $\mathbf{X_r}$ horizontal distance of the return point to the origin, $\mathbf{Y_m}$ vertical distance of the centerline peak to the origin, $\mathbf{Y_t}$ terminal rise height

9 Greek symbols

β saline contraction coefficient, $\mathbf{\Gamma}$ molecular diffusivity, δ Kronecker delta, ϵ, ϵ_ϕ dissipation rate of turbulent kinetic energy, ν molecular viscosity, $\nu_\mathbf{t}$ eddy viscosity, $\mathbf{\Pi_{ij}}$ pressure-strain correlation, $\pi_{\mathbf{i}\phi}$ pressure-scalar correlation, $\rho_\mathbf{0}$ jet density, $\rho_\mathbf{a}, \rho_\mathbf{r}$ water density, $\tau_\mathbf{ij}$ stress tensor, $\mathbf{\Phi}$ scalar quantity, mean scalar quantity, ϕ' scalar fluctuation

References

[1] Roberts, P.J., Salas, H.J., Reiff, F.M., Libhaber, M., Labbe, A., Thomson, J.C.: Marine Wastewater Outfalls and Treatment Systems, (2010)

[2] Roberts, P.J., Ferrier, A., Daviero, G.: Mixing in inclined dense jets. Journal of Hydraulic Engineering **123**(8), 693–699 (1997)

[3] Zeitoun, M., Reid, R., McHilhenny, W., Mitchell, T.: Model studies of outfall systems for desalination plants. Office of Saline Water, US Department of the Interior, Washington DC (1972)

[4] Pincince, A.B., List, E.J.: Disposal of brine into an estuary. Journal (Water Pollution Control Federation), 2335–2344 (1973)

[5] Cipollina, A., Brucato, A., Grisafi, F., Nicosia, S.: Bench-scale investigation of inclined dense jets. Journal of Hydraulic Engineering **131**(11), 1017–1022 (2005)

[6] Kikkert, G.A., Davidson, M., Nokes, R.: Inclined negatively buoyant discharges. Journal of Hydraulic engineering **133**(5), 545–554 (2007)

[7] Papakonstantis, I.G., Christodoulou, G.C., Papanicolaou, P.N.: Inclined negatively buoyant jets 1: geometrical characteristics. Journal of Hydraulic Research **49**(1), 3–12 (2011)

[8] Papakonstantis, I.G., Christodoulou, G.C., Papanicolaou, P.N.: Inclined negatively buoyant jets 2: concentration measurements. Journal of Hydraulic Research **49**(1), 13–22 (2011)

[9] Shao, D., Law, A.W.-K.: Mixing and boundary interactions of 30 and 45 inclined dense jets. Environmental Fluid Mechanics **10**(5), 521–553 (2010)

[10] Lai, C.C., Lee, J.H.: Mixing of inclined dense jets in stationary ambient. Journal of hydro-environment research **6**(1), 9–28 (2012)

[11] Oliver, C., Davidson, M., Nokes, R.: Removing the boundary influence on negatively buoyant jets. Environmental Fluid Mechanics **13**(6), 625–648

(2013)

[12] Oliver, C.: Near field mixing of negatively buoyant jets (2012)

[13] Bashitialshaaer, R., Larson, M., Persson, K.M.: An experimental investigation on inclined negatively buoyant jets. Water **4**(3), 720–738 (2012)

[14] Jiang, B., Law, A.W.-K., Lee, J.H.-W.: Mixing of 30 and 45 inclined dense jets in shallow coastal waters. Journal of Hydraulic Engineering **140**(3), 241–253 (2013)

[15] Abessi, O., Roberts, P.J.: Effect of nozzle orientation on dense jets in stagnant environments. Journal of Hydraulic Engineering **141**(8), 06015009 (2015)

[16] Abessi, O., Roberts, P.J.: Effect of nozzle orientation on dense jets in stagnant environments. Journal of Hydraulic Engineering **141**(8), 06015009 (2015)

[17] Crowe, A., Davidson, M., Nokes, R.: Velocity measurements in inclined negatively buoyant jets. Environmental Fluid Mechanics **16**(3), 503–520 (2016)

[18] Abessi, O., Roberts, P.J.: Dense jet discharges in shallow water. Journal of Hydraulic Engineering **142**(1), 04015033 (2015)

[19] Papakonstantis, I.G., Tsatsara, E.I.: Trajectory characteristics of inclined turbulent dense jets. Environmental Processes **5**(3), 539–554 (2018)

[20] Papakonstantis, I.G., Tsatsara, E.I.: Mixing characteristics of inclined turbulent dense jets. Environmental Processes **6**(2), 525–541 (2019)

[21] Crowe, A.T.: Inclined negatively buoyant jets and boundary interaction. PhD thesis, University of Canterbury (2013)

[22] Tahmooresi, S., Ahmadyar, D.: Application of reynolds flux modeling in cfd simulation of 45° inclined negatively buoyant jets. Environmental Fluid Mechanics, 1–32 (2022)

[23] Mohammadian, A., Gildeh, H.K., Nistor, I.: CFD modeling of effluent discharges: a review of past numerical studies. Water **12**(3), 856 (2020)

[24] Doneker, R.L., Jirka, G.H.: Cormix user manual: A hydrodynamic mixing zone model and decision support system for pollutant discharges into surface waters. US Environmental Protection Agency, Washington DC (2007)

[25] Robinson, D., Wood, M., Piggott, M., Gorman, G.: Cfd modelling

of marine discharge mixing and dispersion. Journal of Applied Water Engineering and Research **4**(2), 152–162 (2016)

[26] Papakonstantis, I.G., Christodoulou, G.C.: Simplified modelling of inclined turbulent dense jets. Fluids **5**(4), 204 (2020)

[27] Crowe, A., Davidson, M., Nokes, R.: Modified reduced buoyancy flux model for desalination discharges. Desalination **378**, 53–59 (2016)

[28] Morton, B., Taylor, G.I., Turner, J.S.: Turbulent gravitational convection from maintained and instantaneous sources. Proceedings of the Royal Society of London. Series A. Mathematical and Physical Sciences **234**(1196), 1–23 (1956)

[29] Fan, L.-N.: Turbulent buoyant jets into stratified or flowing ambient fluids (1967)

[30] Wang, H., Law, A.W.-k.: Second-order integral model for a round turbulent buoyant jet. Journal of Fluid Mechanics **459**, 397–428 (2002)

[31] Jirka, G.H.: Integral model for turbulent buoyant jets in unbounded stratified flows. part i: Single round jet. Environmental Fluid Mechanics **4**(1), 1–56 (2004)

[32] Yannopoulos, P.: An improved integral model for plane and round turbulent buoyant jets. Journal of Fluid Mechanics **547**, 267–296 (2006)

[33] Oliver, C., Davidson, M., Nokes, R.: Predicting the near-field mixing of desalination discharges in a stationary environment. Desalination **309**, 148–155 (2013)

[34] Yannopoulos, P., Bloutsos, A.: Escaping mass approach for inclined plane and round buoyant jets. Journal of fluid mechanics **695**, 81–111 (2012)

[35] Bloutsos, A.A., Yannopoulos, P.C.: Revisiting mean flow and mixing properties of negatively round buoyant jets using the escaping mass approach (ema). Fluids **5**(3), 131 (2020)

[36] Papakonstantis, I.G., Papanicolaou, P.N.: On the computational modeling of inclined brine discharges. Fluids **7**(2), 86 (2022)

[37] Jirka, G.H.: Improved discharge configurations for brine effluents from desalination plants. Journal of Hydraulic Engineering **134**(1), 116–120 (2008)

[38] Vafeiadou, P., Papakonstantis, I., Christodoulou, G.: Numerical simulation of inclined negatively buoyant jets. In: The 9th International Conference on Environmental Science and Technology, September, pp.

1–3 (2005)

[39] Oliver, C., Davidson, M., Nokes, R.: k-ε predictions of the initial mixing of desalination discharges. Environmental Fluid Mechanics **8**(5-6), 617 (2008)

[40] Kheirkhah Gildeh, H., Mohammadian, A., Nistor, I., Qiblawey, H., Yan, X.: CFD modeling and analysis of the behavior of 30 and 45 inclined dense jets–new numerical insights. Journal of Applied Water Engineering and Research **4**(2), 112–127 (2015)

[41] Kheirkhah Gildeh, H., Mohammadian, A., Nistor, I., Qiblawey, H.: Numerical modeling of 30 and 45 degree inclined dense turbulent jets in stationary ambient. Environmental Fluid Mechanics **15**(3), 537–562 (2015)

[42] Tahmooresi, S., Ahmadyar, D.: Effects of turbulent schmidt number on cfd simulation of 45° inclined negatively buoyant jets. Environmental Fluid Mechanics **21**(1), 39–62 (2021)

[43] Ramezani, M., Abessi, O., Firoozjaee, A.R.: Effect of proximity to bed on 30° and 45° inclined dense jets: A numerical study (2021)

[44] Zhang, S., Jiang, B., Law, A.W.-K., Zhao, B.: Large eddy simulations of 45 inclined dense jets. Environmental Fluid Mechanics **16**(1), 101–121 (2015)

[45] Zhang, S., Law, A.W.-K., Jiang, M.: Large eddy simulations of 45 and 60 inclined dense jets with bottom impact. Journal of hydro-environment research **15**, 54–66 (2017)

[46] Jiang, M., Law, A.W.-K., Lai, A.C.: Turbulence characteristics of 45 inclined dense jets. Environmental Fluid Mechanics **19**(1), 27–54 (2019)

[47] Jiang, M., Law, A.W.-K., Song, J.: Mixing characteristics of inclined dense jets with different nozzle geometries. Journal of Hydro-environment Research **27**, 116–128 (2019)

[48] Jiang, M., Law, A.W.-K.: Mixing of swirling inclined dense jets–a numerical study. Journal of Hydro-environment Research **21**, 118–130 (2018)

[49] Vafa, N., Azadi, A., Firoozabadi, B.: Effect of numerical schemes on advection terms for large eddy simulation of inclined dense jets. Environmental Fluid Mechanics, 1–26 (2021)

[50] Palomar, P., Lara, J., Losada, I.: Near field brine discharge modeling part

2: Validation of commercial tools. Desalination **290**, 28–42 (2012)

[51] Rodi, W.: Turbulence Models and Their Application in Hydraulics. Germany: University of Karlsruhe, (1980)

[52] Millero, F.J., Poisson, A.: International one-atmosphere equation of state of seawater. Deep Sea Research Part A. Oceanographic Research Papers **28**(6), 625–629 (1981)

[53] Younis, B.A., Speziale, C.G., Clark, T.T.: A rational model for the turbulent scalar fluxes. Proceedings of the Royal Society A: Mathematical, Physical and Engineering Sciences **461**(2054), 575–594 (2005)

[54] Batchelor, G.: Diffusion in a field of homogeneous turbulence. i. eulerian analysis. Australian Journal of Chemistry **2**(4), 437–450 (1949)

[55] Daly, B.J., Harlow, F.H.: Transport equations in turbulence. The Physics of Fluids **13**(11), 2634–2649 (1970)

[56] Hanjalić, K., Launder, B.: Modelling Turbulence in Engineering and the Environment: Second-moment Routes to Closure. Cambridge university press, (2011)

[57] Launder, B.: Heat and mass transport, chapter 6 in turbulence, ed. by p. bradshaw. Topics in Applied Physics **12** (1976)

[58] Launder, B.: The prediction of force field effects on turbulent shear flows via second-moment closure. In: Advances in Turbulence 2, pp. 338–358. Springer, (1989)

[59] Hossain, M., Rodi, W.: A turbulence model for buoyant flows and its application to vertical buoyant jets. In: Turbulent Buoyant Jets and Plumes, pp. 121–178. Elsevier, (1982)

[60] Monin, A.: On the symmetry properties of turbulence in the surface layer of air. Isv. Atmos. Ocean. Phys. **1**, 45–54 (1965)

[61] Launder, B.: On the effects of a gravitational field on the turbulent transport of heat and momentum. Journal of Fluid Mechanics **67**(3), 569–581 (1975)

[62] Gibson, M., Launder, B.: Ground effects on pressure fluctuations in the atmospheric boundary layer. Journal of Fluid Mechanics **86**(3), 491–511 (1978)

[63] Gibson, M., Launder, B.: On the calculation of horizontal nonequilibrium turbulent shear flows under gravitational influence. Journal of Heat Transfer, 81 (1976)

[64] Speziale, C.G., Sarkar, S., Gatski, T.B.: Modelling the pressure–strain correlation of turbulence: an invariant dynamical systems approach. Journal of fluid mechanics **227**, 245–272 (1991)

[65] Greenshields, C.J.: Openfoam user guide version 6. The OpenFOAM Foundation **237** (2018)

[66] Roberts, P.J., Toms, G.: Inclined dense jets in flowing current. Journal of Hydraulic Engineering **113**(3), 323–340 (1987)

[67] Malin, M., Younis, B.: Calculation of turbulent buoyant plumes with a reynolds stress and heat flux transport closure. International journal of heat and mass transfer **33**(10), 2247–2264 (1990)

[68] Shao, D., Law, A.W.-K.: Turbulent mass and momentum transport of a circular offset dense jet. Journal of Turbulence **10**(10), 40 (2009)

[69] Cresswell, R., Szczepura, R.: Experimental investigation into a turbulent jet with negative buoyancy. Physics of Fluids A: Fluid Dynamics **5**(11), 2865–2878 (1993)